Sodium-Ion Batteries

International Edition: DOI: 10.1002/anie.201911698
German Edition: DOI: 10.1002/ange.201911698

P2-$Na_{0.67}Al_xMn_{1-x}O_2$: Cost-Effective, Stable and High-Rate Sodium Electrodes by Suppressing Phase Transitions and Enhancing Sodium Cation Mobility

Xiangsi Liu[+], Wenhua Zuo[+], Bizhu Zheng, Yuxuan Xiang, Ke Zhou, Zhumei Xiao, Peizhao Shan, Jingwen Shi, Qi Li, Guiming Zhong, Riqiang Fu, and Yong Yang**

Abstract: *Sodium layered P2-stacking $Na_{0.67}MnO_2$ materials have shown great promise for sodium-ion batteries. However, the undesired Jahn–Teller effect of the Mn^{4+}/Mn^{3+} redox couple and multiple biphasic structural transitions during charge/discharge of the materials lead to anisotropic structure expansion and rapid capacity decay. Herein, by introducing abundant Al into the transition-metal layers to decrease the number of Mn^{3+}, we obtain the low cost pure P2-type $Na_{0.67}Al_xMn_{1-x}O_2$ ($x = 0.05$, 0.1 and 0.2) materials with high structural stability and promising performance. The Al-doping effect on the long/short range structural evolutions and electrochemical performances is further investigated by combining in situ synchrotron XRD and solid-state NMR techniques. Our results reveal that Al-doping alleviates the phase transformations thus giving rise to better cycling life, and leads to a larger spacing of Na^+ layer thus producing a remarkable rate capability of 96 mAh g^{-1} at 1200 mA g^{-1}.*

Introduction

Among all secondary batteries, lithium-ion batteries (LIBs) offer the highest energy densities and dominate the market of portable electronics and electric vehicles.[1] However, the rising concerns about the exhaustion and cost of Li resources have driven the scientific community to search for more sustainable electrochemical energy storage systems. Sodium-ion batteries (SIBs) have attracted enormous attention owing to the wide distribution, high natural abundance and potentially low cost of sodium compared to lithium.[2] Given that SIBs have great potential at electrical grid systems,[3] cost, elemental abundance and specific capacity should be the primary considerations for a qualified cathode material. Manganese is an earth-abundant, low-cost, and low-toxic transition metal. Among various cathodes that have been investigated, layered sodium transition metal oxides (Na_xTMO_2), especially Mn-based materials, are considered highly of the potential to meet the above requirements and thus present a great promise for the application of SIBs.[4]

The Na_xMnO_2 layered oxides, have been firstly studied as positive materials of SIBs over 30 years ago[5] while their phase variations[6] had been discussed much earlier. Based on the MnO_2-slab stacking patterns along the *c*-axis, the layered Na_xMnO_2 can be grouped into two polymorphs, namely the O3-type $NaMnO_2$ (ABC oxygen stacking) and the P2-type $Na_{0.67}MnO_2$ (ABBA oxygen stacking) structures. It was reported that O3-type Na_xMnO_2 exhibits poor rate capability and fast capacity degradation because of their unfavored Na^+ diffusion paths and complicated phase-transition processes.[4a,7] In contrast, the distorted P2′-$Na_{0.67}MnO_2$ phase[8] was reported to deliver higher capacities than the undistorted P2-$Na_{0.67}MnO_2$.[9] And unlike $LiMnO_2$, Na_xMnO_2 is hard to transforms from layered phases to spinel structures.[7b,10] Even so, the electrochemical performances of P2/P2′-$Na_{0.67}MnO_2$ are still far from expectations due to the strong Jahn–Teller effect associated with Mn^{3+}/Mn^{4+} redox couple. The presence of Jahn–Teller effect causes P2–P2′ phase transformation thus lowers Na^+ mobility and further leads to stresses, structural defects and amorphization during repeated cycling.[7a,11] Besides, the multiple structure transformations induced by oxygen layer glides were also reported to have detrimental effects on the Na^+ transport and electrochemical reversibility.[7a,12]

A great number of studies have focused on the substitution of the Mn^{3+} Jahn–Teller center by various transition metals in P2/P2′-$Na_{0.67}MnO_2$.[13] One of the most successful examples should be $Na_{0.67}Mg_xMn_{1-x}O_2$.[14] Magnesium is an earth abundant element and very effective to smooth the charge–discharge curves, reduce polarization and improve capacity retention of P2-$Na_{0.67}MnO_2$.[14a] Grey's group showed that Mg-substitution is able to moderate the structural changes and delay the high-voltage phase transition in P2-$Na_{0.67}MnO_2$, by characterizations of solid-state ^{23}Na NMR

[*] X. Liu,[+] W. Zuo,[+] B. Zheng, Y. Xiang, K. Zhou, Z. Xiao, P. Shan, J. Shi, Q. Li, Prof. Dr. Y. Yang
State Key Laboratory for Physical Chemistry of Solid Surfaces, and Department of Chemistry, College of Chemistry and Chemical Engineering, Xiamen University
Xiamen 361005 (P. R. China)
E-mail: yang@xmu.edu.cn
Prof. Dr. Y. Yang
School of Energy Research, Xiamen University
Xiamen 361005 (P. R. China)
G. Zhong
Xiamen Institute of Rare Earth Materials, Haixi institutes
Chinese Academy of Sciences
Xiamen 361021 (P. R. China)
E-mail: gmzhong@fjirsm.ac.cn
Dr. R. Fu
National High Magnetic Field Laboratory
1800 E. Paul Dirac Drive, Tallahassee, FL 32310 (USA)
[+] These authors contributed equally to this work,
Supporting information and the ORCID identification number(s) for the author(s) of this article can be found under: https://doi.org/10.1002/anie.201911698.

spectroscopy, neutron diffraction and X-ray diffraction (XRD).[14b] Improved electrochemical performances were also observed in Li-doped P2-$Na_x(Li_yMn_{1-y})O_2$[15] and Cu-doped P2/P2′-$Na_x(Cu_yMn_{1-y})O_2$.[13,16] Aluminum is the most abundant metal elements in the earth. Its abundance in the continental crust (8.23%) is much higher than Fe (5.63%) and nearly 4-times higher than Mg (2.33%).[4b,17] Once the Al^{3+} are introduced into $Na_{0.67}MnO_2$, the Mn^{3+} Jahn–Teller centers will be reduced. Moreover, the oxygen and Al atoms in the TM layers form the stronger chemical bonds of $501.9 \pm 10\ kJ\,mol^{-1}$ than Mn−O bonds ($362 \pm 25\ kJ\,mol^{-1}$) and Mg−O bonds ($358.2 \pm 7.2\ kJ\,mol^{-1}$).[18] The stronger Al−O chemical bonds in $Na_{0.67}Al_xMn_{1-x}O_2$ will work through the Na-O-Al-O-Na interactions and finally create a broader spacing of the Na^+ layers in of $Na_{0.67}Al_xMn_{1-x}O_2$ than in both $Na_{0.67}MnO_2$ and $Na_{0.67}Mg_xMn_{1-x}O_2$ materials. A larger Na^+ layer-spacing will enhance the Na^+ hopping and leads to a faster Na^+ mobility. Therefore, Al-doping is a suitable strategy to improve the electrochemical performances and to stabilize the structure of $Na_{0.67}MnO_2$. Recently, Al-doped P2-$Na_{0.67}MnO_2$ materials were reported by Wu et al.[19] and Passerini et al.[20] Their results indicate that Al-doping could improve the electrochemical performances of P2-type $Na_{0.67}MnO_2$ materials. However, the hydrated and orthorhombic impurities in their prepared materials certainly influence the electrochemical behaviors of targeted electrode materials.[4a] Moreover, as well as other layered sodium transition metal oxides systems,[21] the in-depth comprehension of the Al-doping mechanisms remains poorly understood.

Herein, we present a systematic investigation on Al-doped P2-$Na_{0.67}Al_xMn_{1-x}O_2$ ($x = 0$, 0.05, 0.1, 0.2) series as cathodes for SIBs. With the increase of Al content, the structures transform from P2′ + P2 ($x = 0$ and 0.05) to the undistorted P2 ($x = 0.1$ and 0.2) phase, due to the gradual reduction of Mn^{3+} Jahn–Teller centers. The Al substitution samples exhibit smoother charge-discharge profiles and the optimized $Na_{0.67}Al_{0.1}Mn_{0.9}O_2$ compound exhibits exceptional electrochemical performances. It delivers high specific capacity of 193 and 175 $mAh\,g^{-1}$ at 0.05 C within 1.5–4.3 and 2.0–4.0 V, respectively; outstanding rate capability with over 50% capacity retention even the current increased 100 times, and long cycling stability exceeding 200 cycles with 85% capacity retention at 480 $mA\,g^{-1}$. The further improvement of Al contents leads to better capacity retentions but lower specific capacities. Furthermore, the structures of powder materials, phase transitions during electrode preparation and electrochemical cycling are investigated in-depth by the combination of long-range (powder and synchrotron XRD) and short-range (ss-NMR) structures characterization techniques. The results reveal that Al-doping could increase Na^+ layers spacing, stabilize the structure during the electrode preparation procedures and prevent the multiple biphasic structure transformations at both charge and discharge, leading to excellent electrochemical performances. The high specific capacity, remarkable rate capability, high cycling stability of $Na_{0.67}Al_{0.1}Mn_{0.9}O_2$ suggest that Al-doped P2-$Na_{0.67}MnO_2$ is promising for large scale energy storage systems.

Results and Discussion

Characterization of $Na_{0.67}Al_xMn_{1-x}O_2$

A series of Al-doped P2-$Na_{0.67}Al_xMn_{1-x}O_2$ ($x = 0$, 0.05, 0.1, 0.2 and 0.3) were prepared by sol-gel method with a quenching process. The morphologies of prepared $Na_{0.67}Al_xMn_{1-x}O_2$ are characterized by SEM and shown in Figure S1 in the Supporting Information. The primary particle size of P2′-$Na_{0.67}MnO_2$ ranges from 2–5 μm, and particle sizes of Al-doped samples are smaller than undoped one with around 1–3 μm in prevail. The ICP-AES results in Table S1 indicate the chemical compositions of the prepared materials are in good agreement with the ratios of reactants. The XRD patterns of these compounds are in Figure 1a and Figure S2. Rietveld refinements were performed with GSAS[22] and the results are shown in Figure S3 and Table S2. The diffraction patterns of $Na_{0.67}MnO_2$ were mainly indexed to orthorhombic lattice with the space group *Cmcm* (JCPDF no. 27-752), which was denoted as P2′-$Na_{0.67}MnO_2$.[9] This material is a distorted phase to hexagonal P2-$Na_{0.67}MnO_2$ (JCPDF no 27-751) due to the presence of large number of Jahn–Teller active Mn^{3+}. Moreover, 30.8 wt% content of hexagonal phase was also observed by Rietveld refinements, as shown in Figure S3a. As the Al content raised to 5 mol%, the refinement results in Figure S3b confirm that the amount of hexagonal phase is increased to 73.9 wt%. With the further increase of Al content, pure P2 phase material is produced. This trend indicates that the distorted Mn^{3+} Jahn–Teller centers are reduced by substituting Mn^{3+} with Al^{3+}. However, the observation of $MnAlO_4$ and $NaAlO_2$ impurities in the XRD pattern of $Na_{0.67}Al_{0.3}Mn_{0.7}O_2$ (Figure S2) suggests that the substitution limit of Al in P2-$Na_{0.67}Al_xMn_{1-x}O_2$ is lower than 30 mol%, at least in the sol-gel method. Therefore, the following research is mainly focused on the $Na_{0.67}Al_xMn_{1-x}O_2$ phases with $x = 0$, 0.05, 0.1, and 0.2. The structure of $Na_{0.67}Al_xMn_{1-x}O_2$ is illustrated in Figure S4. The lengths of Mn−O bonds ($d_{Mn\text{-}O}$ and $d'_{Mn\text{-}O}$) and spacings of Na^+ layers ($d_{O\text{-}Na\text{-}O}$) are calculated from the refinements results and shown in Table 1. The distortion of P2′-$Na_{0.67}Al_{0.05}Mn_{0.95}O_2$ phase is much smaller than that of P2′-$Na_{0.67}MnO_2$, on account of the smaller differences of the anisotropic Mn−O bond lengths, as exhibited in Table 1. With the increasing Al content, P2-$Na_{0.67}Al_xMn_{1-x}O_2$ phases have a shorter $d_{TM\text{-}O}$ because of the smaller ionic radius of Al^{3+} (0.535 Å) than Mn^{3+} (high spin, 0.645 Å). Importantly, the value of Al−O bond strength ($501.9 \pm 10.6\ kJ\,mol^{-1}$) is much higher than Mn−O bonds ($362 \pm 25\ kJ\,mol^{-1}$).[18] The stronger TM−O bond strengths in the configuration of O-Na-O-TM-O-Na-O along *c*-axis could weaken the O−Na−O bond strengths, leading to broader spacings of Na^+ layers. As a result, the $d_{O\text{-}Na\text{-}O}$ broadens with the introduction of Al, as evidenced in Table 1. It indicates that the prepared $Na_{0.67}Al_xMn_{1-x}O_2$ ($x \geq 0$) would exhibit faster Na^+ mobilities with the increasing Al^{3+} content.

The ^{23}Na ss-NMR was performed to study the local Na^+ environment of powder $Na_{0.67}Al_xMn_{1-x}O_2$. For convenience, we removed the sidebands by using the pj-MATPASS pulse sequence[23] and the resulting spectra are shown in Figure 1b.

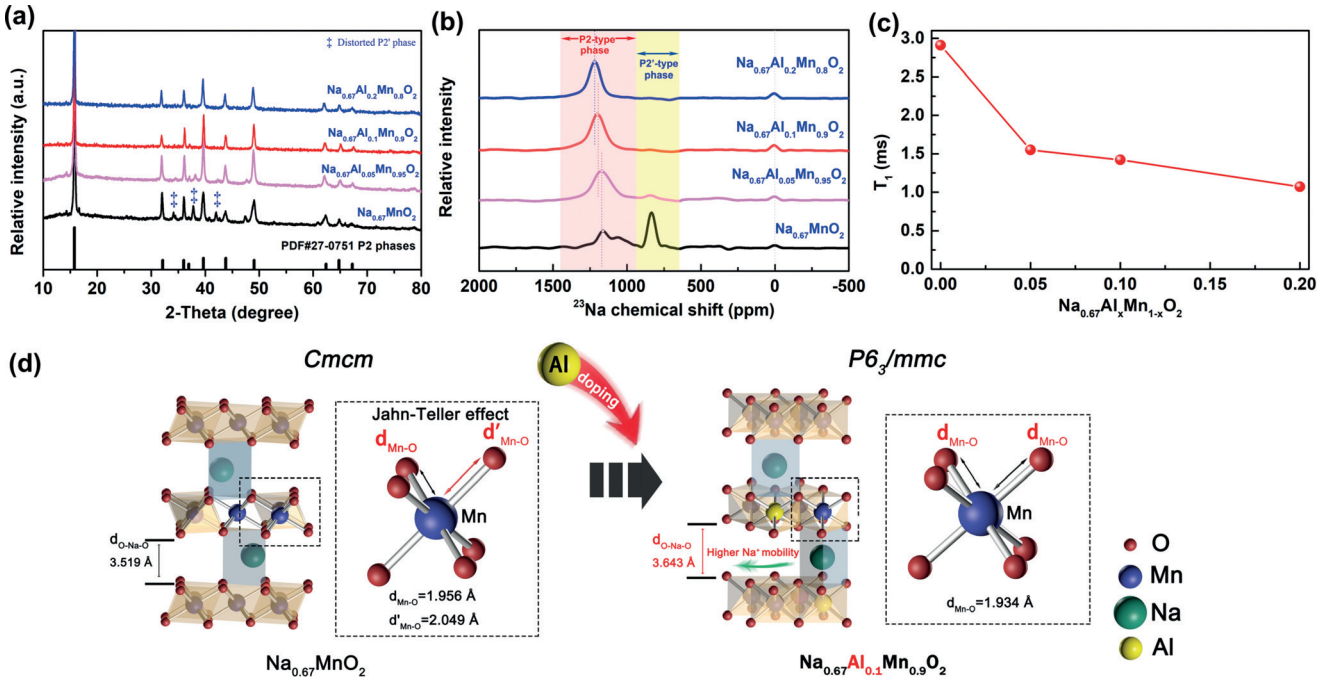

Figure 1. Structural characterizations. a) Powder XRD, b) ^{23}Na ss-NMR spectra and c) the fitting results of T_1 value of prepared materials. d) Schematic illustration of effects of Al^{3+} doping on electrode structures.

Table 1: The lengths of Mn(Al)—O bonds and spacings of Na^+ layers from Refined crystallographic parameters for prepared materials.

P2-$Na_{0.67}Al_xMn_{1-x}O_2$	$x=0$		$x=0.05$		$x=0.1$ (P2)	$x=0.2$ (P2)
	P2′	P2	P2′	P2		
d_{Mn-O}	1.956	1.966	1.963	1.955	1.934	1.926
d'_{Mn-O}	2.049	1.966	1.989	1.955	1.934	1.926
d_{O-Na-O}	3.519	3.466	3.703	3.554	3.643	3.694

The signals located at 650–900 ppm and 900–1400 ppm are assigned to Na^+ in P2′ and P2 phases, respectively. The signals at 0 ppm are due to the diamagnetic sodium salts, such as Na_2CO_3, which are formed in the manufacture processes and will be not discussed in the following part. For the undoped $Na_{0.67}MnO_2$ material, two distinctive signals with a sharp one located at 835 ppm and wide one at 1162 ppm are observed in the spectrum, indicating that $Na_{0.67}MnO_2$ is dominated by P2′ with some P2 phases. This correspondence relationship between the signals of ss-NMR and crystal structure is further confirmed in the following. The splitting peak in P2′ phase region is caused by the quadrupolar interaction possibly, which comes from the quadrupolar nucleus ^{23}Na in an asymmetrical local environment.[24] After doping with Al^{3+}, only P2 signals can be observed in the spectra, which reveals that Al^{3+} doping can reduce the Mn^{3+} Jahn–Teller centers, as well as rearrange the local structures to form P2 phases. Furthermore, the chemical shift move to lower field with increasing Al^{3+} amounts, indicating that the average valence of Mn-ion increases gradually.[25] To further evaluate the Na^+ (de)intercalation dynamics of $Na_{0.67}Al_xMn_{1-x}O_2$, the T_1 (spin-lattice relaxation times) of the materials were obtained by the saturation recovery method and the fitting results are shown in Table S3. For paramagnetic materials, the stronger electron-dipolar interactions and faster Na^+ jump rates lead to lower T1 values. As shown in Figure 1c and Table S3, the obtained T_1 value of 6.04 ms for the P2′ phase (750–900 ppm, Mn^{3+}-dominated) is much higher than 2.91 ms of the P2 (900–1400 ppm, Mn^{4+}-dominated) phase, which contradicts with the fact that Mn^{3+} ($t_{2g}3$, e_g1) has a stronger electron-dipolar interaction than Mn^{4+} ($t_{2g}3$) thus confirms the faster Na^+ mobility of the P2 phase than P2′ phase. Similarly, due to the improvement of Na^+ diffusion coefficient, the T_1 value from the signal at 900 to 1400 ppm in the ^{23}Na NMR spectrum of $Na_{0.67}Al_{0.05}Mn_{0.95}O_2$ material is only half that of $Na_{0.67}MnO_2$ (Figure 1c) and further decreases with the increase of Al^{3+} contents. In summary, Al^{3+}-doping reduces the Mn^{3+} Jahn–Teller centers and expands the interspacing of Na^+ layers and accelerates the movement of Na^+, as schematically illustrated in Figure 1d.

Electrochemical Properties of $Na_{0.67}Al_xMn_{1-x}O_2$

To evaluate the electrochemical properties of $Na_{0.67}Al_xMn_{1-x}O_2$ cathodes, galvanostatic charging-discharging experiments were performed in Na half cells with PC-$NaClO_4$ as electrolyte. As shown in Figure 2a and Figure S6–7, compared with $Na_{0.67}MnO_2$, the Al-substituted samples exhibit much smoother charge–discharge profiles, even with only 5 mol% Al^{3+} in TM layers. This evidences that the introduction of Al disrupts the existence of biphasic domains, which are related to the TM ordering in the TM layers and obstruct Na^+-vacancy ordering during (de)intercalation processes.[7a,14a] At 12 mA g^{-1} within 2.0–4.0 V (Figure 2a and Figure S6), the initial discharge capacities of the prepared

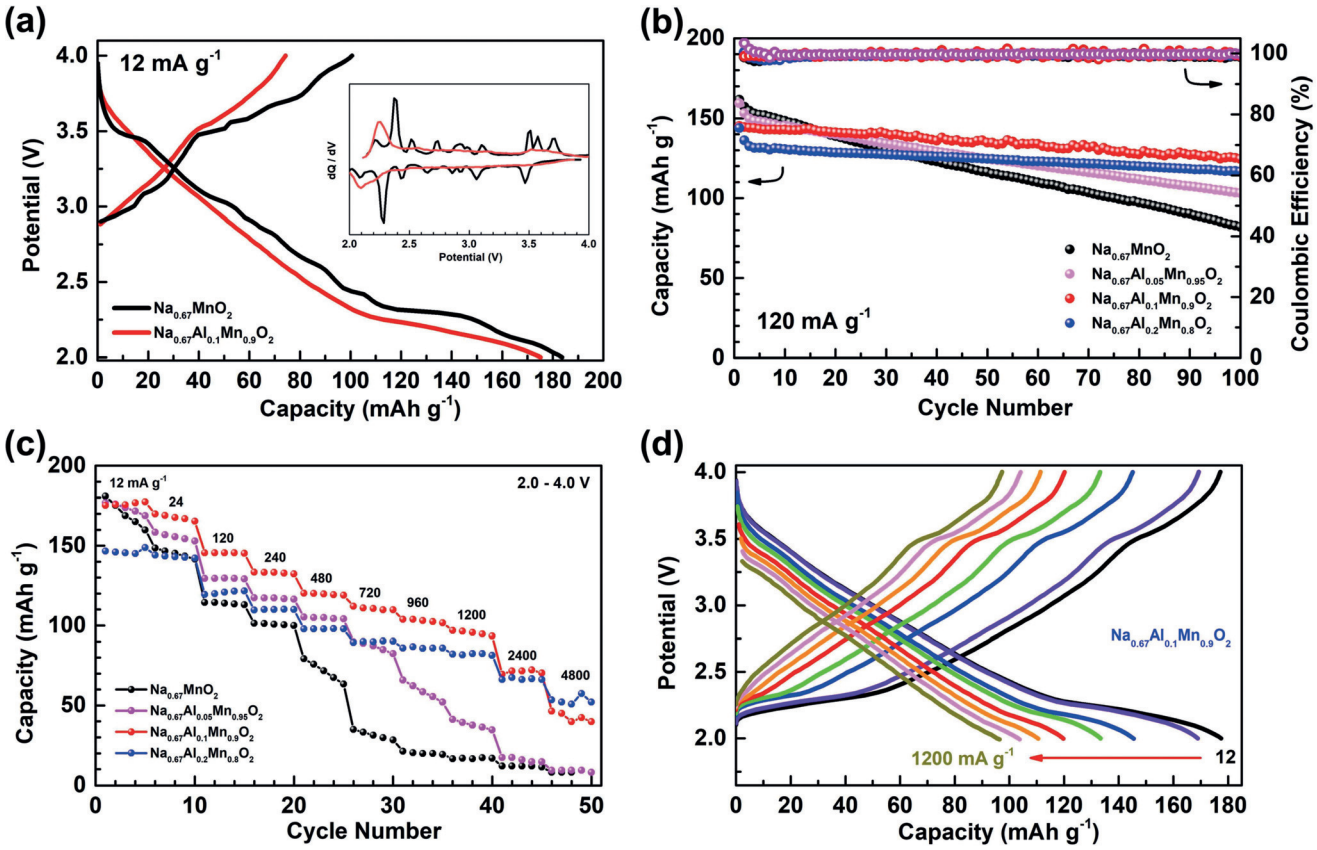

Figure 2. Electrochemical performances of $Na_{0.67}Al_xMn_{1-x}O_2$ in the potential range of 2.0–4.0 V. a) Charge/discharge curves and *dQ/dV* profiles (Inset) at the second cycle of $Na_{0.67}MnO_2$ and P2-$Na_{0.67}Al_{0.1}Mn_{0.9}O_2$ at 12 mA g^{-1}. b) Cycling stabilities at 120 mA g^{-1} of the synthesized materials. c) Rate capabilities of prepared electrodes, which tested by charging at 24 mA g^{-1} and discharging at the current densities ranging from 12–4800 mA g^{-1}. d) Charge/discharge curves of P2-$Na_{0.67}Al_{0.1}Mn_{0.9}O_2$ at different current densities (charge at 24 mA g^{-1} and discharge at 12–4800 mA g^{-1}).

$Na_{0.67}Al_xMn_{1-x}O_2$ materials are 183, 176, 175, and 148 mAh g^{-1} for $x=0$, 0.05, 0.1, and 0.2, respectively. 10 mol% Al-doping sample exhibit only 7–8 mAh g^{-1} compromised capacities as compared to $Na_{0.67}MnO_2$ electrode. When working potential range expanded to 1.5–4.3 V (Figure S7), the capacities delivered by $Na_{0.67}Al_xMn_{1-x}O_2$ are 215, 202, 198, and 161 mAh g^{-1} for $x=0$, 0.05, 0.1, and 0.2, respectively. The cycling performances of the prepared $Na_{0.67}Al_xMn_{1-x}O_2$ at the constant current densities of 120 and 480 mA g^{-1} are shown in Figure 2b and Figure S8–9. After 100 cycles at 120 mA g^{-1}, the discharge capacities for $x=0$, 0.05, 0.1, and 0.2 are 82, 103, 125, and 116 mAh g^{-1}, and the corresponding capacity retentions are 50%, 69%, 86%, and 88%, respectively. Although the capacity retention improves with the increase of Al content, the capacity of 20 mol% Al^{3+} doped sample is much considerably compromised. Therefore, the electrode with $x=0.1$ shows best cycling performance at 120 mA g^{-1}. Figure S8 displays the charge-discharge plots for the specific cycles of $Na_{0.67}MnO_2$ and $Na_{0.67}Al_{0.1}Mn_{0.9}O_2$. It is clearly observed that, the discharge curves of $Na_{0.67}Al_{0.1}Mn_{0.9}O_2$ electrode after 100 cycles remain nearly the same as that in the 1st cycle. The calculated energy-retentions of $Na_{0.67}MnO_2$ and $Na_{0.67}Al_{0.1}Mn_{0.9}O_2$ after 100 cycles are 52% and 90%, respectively, indicating that the Al-substituted samples also exhibit greatly improved energy-retention capability. At a higher current density of 480 mA g^{-1} (Figure S9), 84% of the initial capacity of $Na_{0.67}Al_{0.1}Mn_{0.9}O_2$ is retained after 200 cycles while only 40% for $Na_{0.67}MnO_2$ under the same condition.

To further investigate the electrochemical performances of prepared materials, the rate capabilities were investigated and the results are shown in Figure 2c,d. Note that the main markets for sodium-ion batteries are electrical grid systems, which store the electricity during the off-peak period while releases it during the peak period of the electricity consumption. As a result, the requirement for the discharge rates of sodium-ion batteries is much higher/faster than charge. Therefore, as well as the previous researches,[14b,26] the rate capabilities are tested by charging at low current and discharging at various currents. Specifically, the cells were charged at a constant current density of 24 mA g^{-1} and discharged at 12–4800 mA g^{-1}, respectively. $Na_{0.67}Al_{0.1}Mn_{0.9}O_2$ provides the best rate capability and stable capacities at each current density (Figure 2c). The initial discharge capacity of $Na_{0.67}Al_{0.1}Mn_{0.9}O_2$ is 175 mAh g^{-1} at 12 mA g^{-1}. This electrode can maintain 96%, 83%, 69%, and 55% of the initial capacity when the discharge current density increased by 2, 10, 40, and 100 fold, respectively. Even with 200 and 400 times increase of the current density, the capacity retention is up to 40% (70 mAh g^{-1}, 105 s discharge time) and 30%

(52 mAh g^{-1}, 39 s discharge time), respectively, indicating excellent rate capability. The $Na_{0.67}Al_xMn_{1-x}O_2$ materials with $x=0$, 0.05 and 0.1 yield the comparable initial specific discharge capacities at the current density of 12 mA g^{-1}. However, the capacity of undoped and 5 mol% Al-doping phases drops significantly in the first 5 cycles. At the current density of 720 mA g^{-1}, the delivered capacities of samples with $x=0$, 0.05 and 0.2 are 31, 87, and 89 mAh g^{-1}, corresponding to 28%, 78%, and 80% of discharge capacity of $Na_{0.67}Al_{0.1}Mn_{0.9}O_2$, respectively. With further increasing current densities, the undoped and 5 mol% Al-doping materials exhibit severer capacity decay. Whereas the $Na_{0.67}Al_{0.2}Mn_{0.8}O_2$ material achieves comparable and even higher discharge capacities in comparison with $Na_{0.67}Al_{0.1}Mn_{0.9}O_2$ at ultra-high current densities of 2400 and 4800 mA g^{-1}, respectively. Selected galvanostatic charge-discharge profiles of the $Na_{0.67}Al_{0.1}Mn_{0.9}O_2$ electrode at different current densities are shown in Figure 2d and Figure S10. The charge-discharge curves exhibit almost similar shapes, revealing good electrochemical reversibility. The lost capacities at higher current densities compared to low current density of 12 mA g^{-1} is focused on the potential below 2.3 V (Figure 2d), which indicate that the electrochemical reactions within 2.0–2.3 V exhibit the sluggish kinetics in the potential range of 2.0–4.0 V. The improved cycling stability and rate capability of Al-substituted samples can be attributed to the prevented phase transformation associated with Na^+-vacancy ordering and improved charge transport due to the increased spacing of Na^+ layers.

Previous works by Bruce's group[14a] and Grey's group[14b] showed that 5 mol% Mg^{2+}-doped $Na_{0.67}Mg_{0.05}Mn_{0.95}O_2$ also exhibits very extraordinary rate performance. To compare the effect of Mg^{2+}-doping and Al^{3+}-doping strategies on the rate capabilities, the $Na_{0.67}Mg_{0.05}Mn_{0.95}O_2$ material was prepared by sol-gel method as the same as $Na_{0.67}Al_{0.1}Mn_{0.9}O_2$ samples. The powder XRD pattern of the prepared $Na_{0.67}Mg_{0.05}Mn_{0.95}$ material (Figure S11a) is very similar to the literatures[14a,b] and no hydrated peaks can be observed. As the comparison of rate capabilities in Figure S11b shows, at the low current density of 12 mA g^{-1}, the comparable initial discharge capacities of 174 and 175 mAh g^{-1} are delivered by the $Na_{0.67}Mg_{0.05}Mn_{0.95}$ and $Na_{0.67}Al_{0.1}Mn_{0.9}O_2$ electrodes, respectively. However, the capacity of $Na_{0.67}Al_{0.1}Mn_{0.9}O_2$ electrode is always higher than $Na_{0.67}Mg_{0.05}Mn_{0.95}O_2$ electrode at the current densities ranging from 24–1200 mA g^{-1}. At the high current density of 1200 mA g^{-1}, the discharge capacity of 5% Mg^{2+}-doped sample is 62 mAh g^{-1} which is only 65% of the $Na_{0.67}Al_{0.1}Mn_{0.9}O_2$ electrode at the same condition. The above results indicate that in the same preparing procedures and testing conditions, Al^{3+}-doped electrode exhibits better rate capability than Mg^{2+}-doped electrode, which is believed to be the result of the stronger bond strength of Al–O bond (501.9 ± 10 kJ mol^{-1}) than Mg–O bonds (358.2 ± 7.2 kJ mol^{-1}).[18]

Changes in Crystal Structures during Electrode Preparation

To gain more insights into the mechanisms of Al-doping, the structural transformations of the $Na_{0.67}MnO_2$ and $Na_{0.67}Al_{0.1}Mn_{0.9}O_2$ samples during electrode preparing processes were investigated by ss-NMR and XRD measurements. The preferential orientation is observed in both $Na_{0.67}MnO_2$ and $Na_{0.67}Al_{0.1}Mn_{0.9}O_2$ electrodes because of the electrode preparation mode, as the XRD data in Figure 3a shows. Moreover, the XRD data of the $Na_{0.67}MnO_2$ uncovered a phase transformation from *Cmcm* (P2′-type) phase to a *C*2/*c* phase during the electrode preparing processes, as evidenced by the XRD peaks marked with "‡" and "†" in Figure 3. While the XRD data of $Na_{0.67}Al_{0.1}Mn_{0.9}O_2$ powder and electrode is the same except substrate (Al) signals. Similar phenomena are observed in the ^{23}Na NMR spectra. As shown in Figure 3b, the local Na^+ environment in the powder is the same as that in the electrode of $Na_{0.67}Al_{0.1}Mn_{0.9}O_2$. However, there are apparent differences between the NMR signals in the powder and electrode of $Na_{0.67}MnO_2$. Firstly, the signal of Mn^{3+} dominated region at 650–900 ppm vanishes and two new peaks emerge in the Mn^{4+} dominated region (correspond to

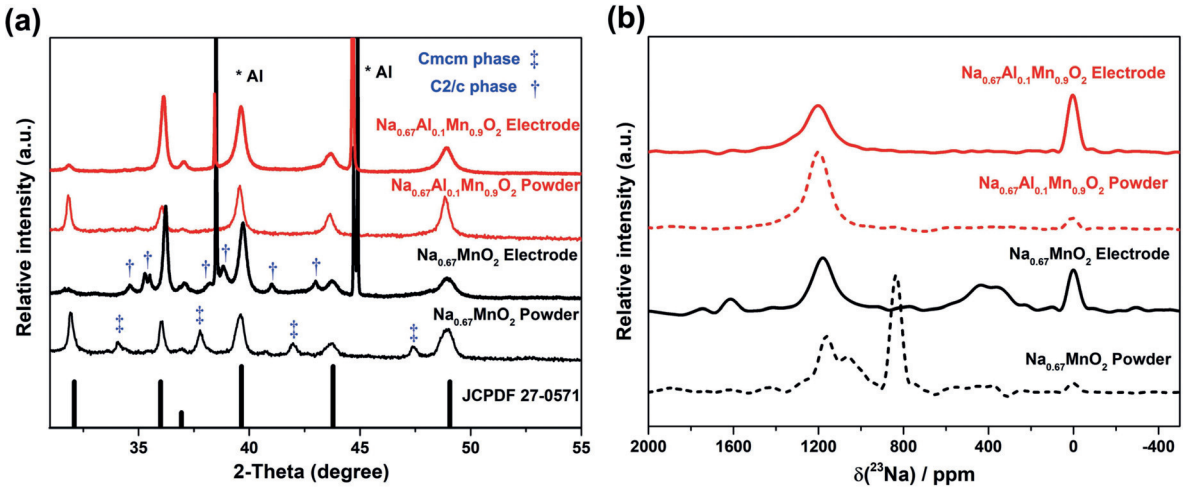

Figure 3. Structure changes in the electrode preparing procedures. The a) XRD and b) NMR spectroscopy data of powder and electrodes of $Na_{0.67}MnO_2$ and $Na_{0.67}Al_{0.1}Mn_{0.9}O_2$. See text for details.

*C*2/*c* phases) at 1400–1850 ppm.[14b] Moreover, the hydrated peak, arising from H_2O inserting into Na^+ layers of the layer structure, appears at 250–600 ppm.[27] The above XRD and NMR results suggest that P2′ phase is unstable and easily transformed into lower symmetrical phases in the electrode preparing procedure. It is well known that P2-phase is more stable than P2′-phase at room temperature,[9] and the commonly adopted ball-milling step in the electrode preparing procedure may provide mechanical energy for *Cmcm*–*C*2/*c* phase transition.

Long-Range Structural Transformations during Charging–Discharging

In situ synchrotron XRD was also employed to track the phase transformations of $Na_{0.67}MnO_2$ and $Na_{0.67}Al_{0.1}Mn_{0.9}O_2$ electrodes in the initial cycle within 2.0–4.0 V. Seven different stages (marked with ①-⑦ in Figure 4a).can be clearly observed in the XRD patterns of $Na_{0.67}MnO_2$. As indicated above, during electrode preparation process, the P2′-phase (space group: *Cmcm*) of $Na_{0.67}MnO_2$ sample turns to a lower symmetric phase with space group of *C*2/*c*, which is denoted as $(C2/c)^1$ in the ① stage. As Na^+ extraction, the intensities of (110), (022), (11$\bar{3}$), (200) and (20$\bar{2}$) peaks disappear and the (023) and (116) peaks shift to higher angles in $x = 0.55$ in Na_xMnO_2, demonstrating that $(C2/c)^1$ changes into a new $(C2/c)^2$ phase by a biphasic process from the ① stage to the ② stage. In $x = 0.46$, the $(C2/c)^2$ phase transforms into $(C2/c)^3$ phase (③ stage) with (023) and (116) peaks further shift to higher angles and the diffraction peaks of $(C2/c)^3$ phase are finally disappeared in $x = 0.29$. The P2-phase in the prepared electrode (space group: *P6₃/mmc*) is maintained in the whole charge process, and all $(C2/c)^3$ phase transforms into P2-phase

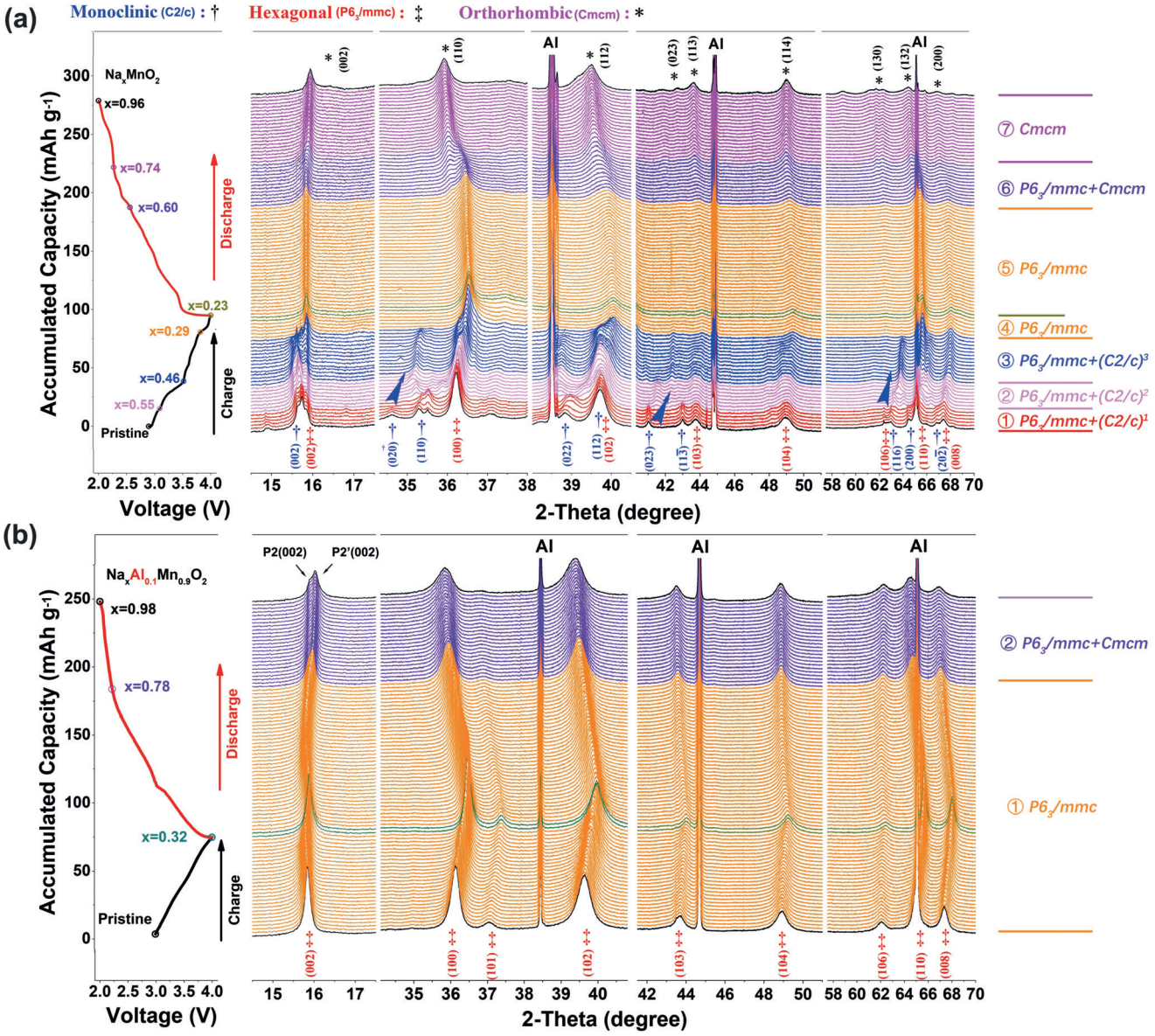

Figure 4. In situ synchrotron XRD during the initial charge–discharge cycle of a) $Na_{0.67}MnO_2$ and b) $Na_{0.67}Al_{0.1}Mn_{0.9}O_2$. The cycling curves are shown at the left of each pattern. The electrode phases are shown at the right of each pattern.

at the ④ stage. The cell parameters of three different *C*2/*c* phases at the specific Na contents are calculated and the results are shown in Table S4. With the Na^+ deintercalation, the β-angle decreases and approaches 90° indicates that the monoclinic distortion of P2-type structure is decreased. The expansion of c lattice parameter is caused by the increase of repulsive electrostatic interactions of O^{2-} with the extraction of Na^+. During the discharge process, P2 and P2′ phases are observed in $0.23 < x < 0.60$ and $0.74 < x < 0.96$, respectively. In the mixed two-phase stage (⑥),the (110) peak of P2 phase disappears and that of P2′ phase emerges gradually indicating a two-phase reaction mechanism of P2–P2′ transformation in the discharge process of $Na_{0.67}MnO_2$ electrode.

Unlike the complexity of structural evolutions of $Na_{0.67}MnO_2$, the operando XRD patterns of $Na_{0.67}Al_{0.1}Mn_{0.9}O_2$ electrode in Figure 4b present much more moderate structure transition. As can be seen, the P2-phase is maintained during the whole charge process and the discharge processes ranging from $0.32 < x < 0.78$. With the further insertion of Na^+, the (002) peak splits into two peaks, indicating the coexistence of P2 (*P63/mmc*) and P2′ (*Cmcm*) phases at the end of discharge, investigated in detail by ex situ ^{23}Na NMR spectroscopic characterization below. The evolution of the lattice parameters of $Na_{0.67}Al_{0.1}Mn_{0.9}O_2$ electrode during the first cycle is calculated and plotted in Figure S13. The lattice parameter *a* shows a monotonous decrease in the charge process and then increases upon Na^+ intercalation, due to the contraction and expansion of MnO_6 octahedron upon the oxidation and reduction of $Mn^{3+/4+}$ redox couples, respectively. The parameter *c* first increases till $x = 0.44$ in $Na_xAl_{0.1}Mn_{0.9}O_2$ due to the increasing electrostatic repulsion of the adjacent oxygen layers upon Na^+ extraction. Then, the contraction in lattice parameter *c* is observed with the further removal of Na^+ because of the slight glides of Mn(Al)-O_2 slabs, as a result of alleviating the repulsion force between neighboring oxygen ions. During discharge process, the change of *c* lattice parameters reverse directions and the lattice parameters of P2′ phase have similar tendency to that of P2 phase. The relative volume change of $Na_xAl_{0.1}Mn_{0.9}O_2$ is only 3.0% during discharge, which is beneficial to its cycling performance.

Local Structure Evolution upon Na^+-(De)intercalation

To further explore the mechanisms of the improvement of electrochemical performance for Al^{3+}-doping, ex situ NMR spectroscopy was performed to characterize the local structure evolutions of $Na_{0.67}MnO_2$ and $Na_{0.67}Al_{0.1}Mn_{0.9}O_2$ electrodes during charge and discharge processes. As mentioned above, the NMR signals located at around 250–600, 650–900, 900–1400, and 1400–1850 ppm correspond to the hydrated, P2′, P2, and *C*2/*c* phases, respectively. The hydrated signal is prone to appear in undoped material at high voltage suggests that layered sodium transition metal oxides with lower sodium content are more vulnerable to water and Al-doping could be beneficial to suppresses the insertion of H_2O in Na^+ layers. The ex situ ^{23}Na NMR spectra of $Na_{0.67}MnO_2$ in the first and second charge/discharge cycles are presented in Figure 5a. In the first charge process, the intensity of the P2 phase signal at 1190 ppm decreases, while the intensity of *C*2/*c* phase signal at 1620 ppm increases and moves towards the lower field gradually, which corresponds to the oxidation of Mn^{3+}. In the first discharge process, the ^{23}Na NMR spectra are almost reversed to that in the charge process as the Na content is lower than 0.68 ($x < 0.68$), demonstrating a rever-

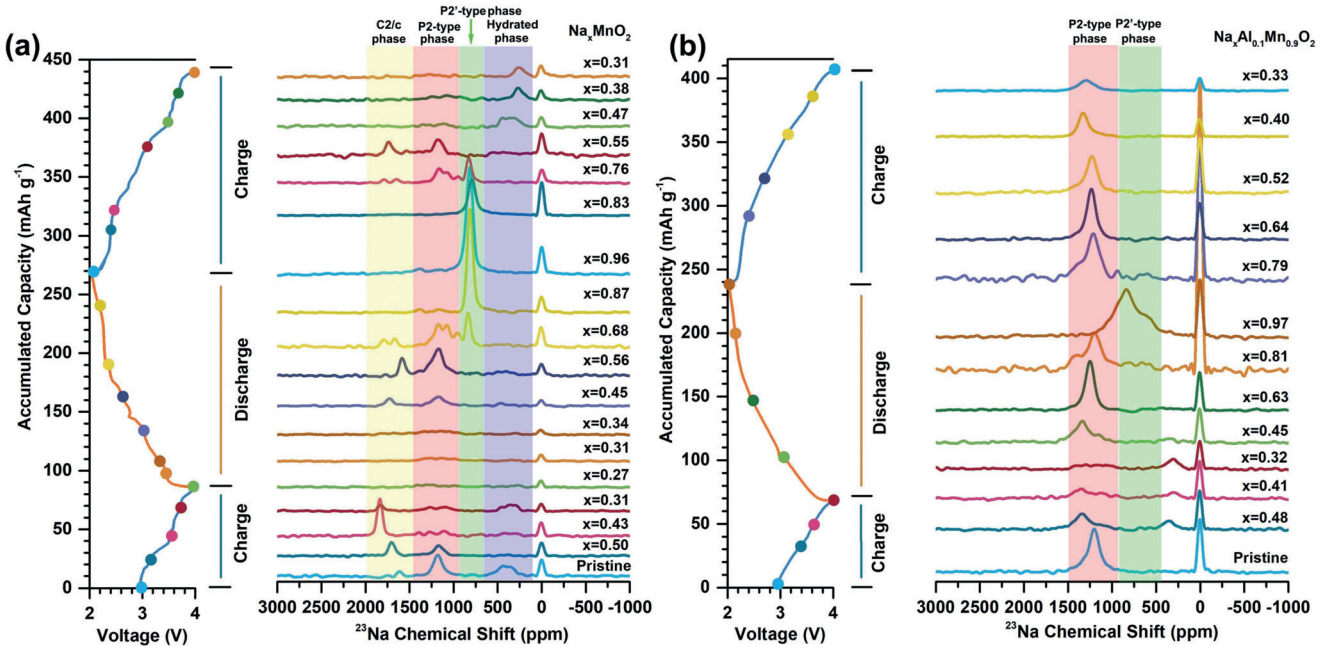

Figure 5. Ex situ ^{23}Na NMR spectra during the initial charge–discharge cycles of a) $Na_{0.67}MnO_2$ and b) $Na_{0.67}Al_{0.1}Mn_{0.9}O_2$. The cycling curves are shown at the left of each spectrum. Na content are represented by *x* and shown at the right of each spectrum. Yellow = *C*2/*c*, pink = P2, green = P2′ and blue colored correspond hydrated phases.

sible electrochemical process. With the further intercalation of Na^+, a new sharp Mn^{3+}-rich signal (corresponding to P2′ phase) at 825 ppm is observed and its intensity becomes stronger due to the increasing of Mn^{3+} sites. Simultaneously, the intensities of the NMR signals corresponding to the *C*2/*c* and P2 phases decrease. Only P2′ signal is observed as the material is fully discharged ($x \geq 0.87$). In the second charge process, the P2′ phase at 825 ppm gradually decrease in intensity and totally disappear as x is lowered to 0.55. Meanwhile, the *C*2/*c* and P2 phase signals recover when $x \leq 0.76$ and become weaker as $x \leq 0.47$. Moreover, the glides of oxygen layers at low Na content lead to many local Na^+ environments or stacking faults, which finally result in a broader signal at around 1100 ppm, as shown in Figure S14.[14b] In contrast to $Na_{0.67}MnO_2$, the *C*2/*c* phase signal is absent in the ^{23}Na NMR spectrum of pristine $Na_{0.67}Al_{0.1}Mn_{0.9}O_2$ electrode in Figure 5b. More importantly, the P2′-phase at 650–900 ppm emerges at $x = 0.68$ in the first discharge process and disappears at $x = 0.55$ in the second charge process for $Na_{0.67}MnO_2$. While for $Na_{0.67}Al_{0.1}Mn_{0.9}O_2$ electrode, the P2′ phase can only be observed as $x = 0.97$. The above NMR results confirm that 10% Al substitution leads to milder and more uniform local structure evolutions during cycling, leading to less structural distortion especially at the highest and lowest Na contents.

From the above NMR and XRD results, the structure evolutions upon Na^+ extraction/intercalation of the $Na_{0.67}MnO_2$ and $Na_{0.67}Al_{0.1}Mn_{0.9}O_2$ electrodes are summarized and illustrated in Figure 6. The $Na_{0.67}MnO_2$ electrode is dominated by severe biphasic transitions during the Na^+ (de)intercalation, involving the evolution of *C*2/*c* structures and P2–P2′ transformation during Na^+ (de)intercalation (Figure 6a). Although NMR results of $Na_{0.67}MnO_2$ electrode is consistent with the XRD patterns, slight discrepancy occurs at the first discharge process. As shown in Figure 5a, the *C*2/*c* phase emerges at $0.45 < x < 0.87$ in the initial discharge process, while no significant phase change is observed in the corresponding XRD patterns. We speculate that this phenomenon is caused by the smaller size of these *C*2/*c* phase than the detection limit of XRD, since the NMR and XRD characterizations reflects the local and long-range structures, respectively. For $Na_{0.67}Al_{0.1}Mn_{0.9}O_2$ electrode, both NMR and XRD results exhibit more moderate structural evolution than

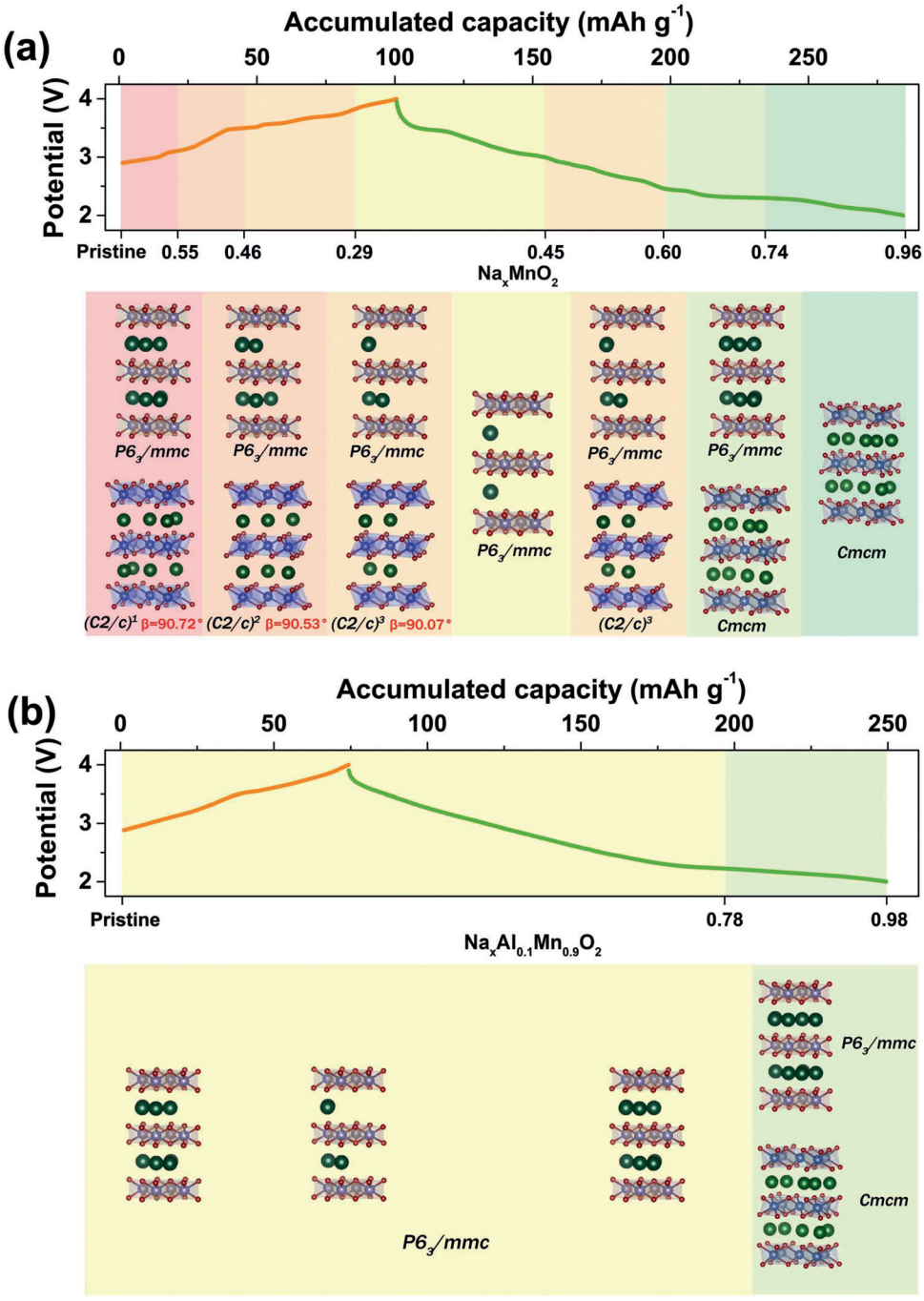

Figure 6. Schematic illustration of structure evolutions of a) $Na_{0.67}MnO_2$ and b) $Na_{0.67}Al_{0.1}Mn_{0.9}O_2$ electrodes.

$Na_{0.67}MnO_2$ electrode (Figure 6a,b). It is important to point out that the synchrotron in situ XRD is insufficient to verify the P2–P2′ phase transition at the end of initial discharge, because the split of (002) peak could be resulted from the two P2 phases with different Na contents. While this structure transformation is clearly confirmed by the ex situ NMR spectra, in which both P2 and P2′ phases can be clearly observed in $x = 0.81$ and 0.97 at the end of initial discharge. The electrochemical signature is more sensitive to the local structures. The structural evolution results correlate well with the shape of the electrochemical charge–discharge curves. Moreover, the galvanostatic intermittent titration (GITT) technique was employed to understand the influence of complex phase transformations on the diffusion coefficient of Na^+ (D_{Na+}). The GITT profiles and D_{Na+} results are plotted in Figure S15 as a function of the Na content x. Despite the apparent difference of geomean values of D_{Na+} between $Na_{0.67}MnO_2$ ($3.32 \times 10^{-11}\ cm^2 s^{-1}$ for charging, $3.76 \times 10^{-11}\ cm^2 s^{-1}$ for discharging) and $Na_{0.9}Al_{0.1}Mn_{0.9}O_2$ (charge: $9.28 \times 10^{-11}\ cm^2 s^{-1}$, discharge: $6.01 \times 10^{-11}\ cm^2 s^{-1}$) electrodes, the evolution characteristics of D_{Na+} versus x are significantly different. For the $Na_{0.67}MnO_2$ electrode, the ①-⑧ stages (in Figure S15a) are marked according to the phase evolution results according to both ex situ NMR and in situ XRD characterizations (Figure 6). The calculated diverging minima located at $x = 0.55$, 0.47, 0.32 during charge and $x = 0.44$, 0.59 and 0.77 during discharge coincides well with the phase boundaries, which suggests that these transitions between two structures lower the Na^+ diffusion coefficients significantly by 1–3 orders of magnitude. For $Na_{0.67}Al_{0.1}Mn_{0.9}O_2$ electrode, the D_{Na+} values increase firstly at the beginning of the initial charge process but decrease at that of the following cycles (Figure S15). The similar phenomenon is also observed in $Na_{0.67}MnO_2$ electrode (Figure S15 and Figure S16). Indicating that the prepared electrodes undergo an activation process at the start of the first cycle. After activation, the D_{Na+} versus x profile exhibits downward sloping shape during both charge and discharge processes, in good accordance to the one-phase characteristics during charge and the mild P2–P2′ phase transformation during discharge. The GITT results suggests that biphasic phase transition of $Na_{0.67}MnO_2$ hinders the diffusion of Na^+ and leads to poor rate capability as well as large voltage hysteresis. Moreover, repeated phase transformation leads to various structural defects and accumulated amorphization, results in inferior cycling stability.[7a] The above problems are significantly mitigated in Al^{3+}-substituted $Na_{0.67}Al_{0.1}Mn_{0.9}O_2$ electrode because of its quasi-single-phase behavior upon Na^+ (de)intercalation.

Conclusion

In summary, the cost-effective P2-$Na_{0.67}Al_xMn_{1-x}O_2$ ($0 \le x \le 0.3$) materials have been developed by a sol-gel and post-quenching approach. In contrast to Mn–O and Mg–O bonds, the stronger Al–O bonds lead to larger sodium spacing thus facilitate Na^+ mobility and stabilize the structure at electrode-preparing processes. Ex situ ^{23}Na NMR spectroscopy and Synchrotron in situ XRD results are in excellent agreement, providing evidence in the advantages of the delayed Jahn–Teller effect of the P2–P2′ phase transition and the suppressed biphasic structural transformations during Na^+ (de)intercalation as Al is introduced into the transition metal layers. The enhanced Na^+ diffusion coefficients, stable frameworks, and delayed structural evolutions ensure excellent rate capability as well as outstanding cycling performance. As a result, without any other modifications, the $Na_{0.67}Al_{0.1}Mn_{0.9}O_2$ compound delivers a high capacity of 175 $mAh\,g^{-1}$ at 12 $mA\,g^{-1}$ within 2.0–4.0 V; When the discharge current densities increased by 100 and 400 fold, the capacities reach 96 $mAh\,g^{-1}$ (144 s discharging time) and 52 $mAh\,g^{-1}$ (11.2 $kW\,kg^{-1}$, discharging in 39 s), respectively, which are exceptional rate and power capabilities. This work presents an effective strategy and provides in-depth insights into the advanced high-power and sustainable layered cathodes based on earth abundant elements for sodium-ion batteries.

Acknowledgements

This work was financially supported by National Key Research and Development Program of China (grant no. 2018YFB0905400, 2016YFB0901502, 2018YFB0905402), National Natural Science Foundation of China (grant no. 21233004, 21428303, 21621091, 21603231, 21761132030, 21875196, 21935009). W.Z. and Y.X. acknowledge the scholarship from Huawei Technologies Co., Ltd. R.F. thanks to the support from the National High Magnetic Field Laboratory, which is supported by NSF Cooperative Agreement NSF/DMR-1644779 and the State of Florida. We are very grateful for the beam time and assistance from scientists at beamlines BL14B1 in Shanghai Synchrotron Radiation Facility (SSRF).

Conflict of interest

The authors declare no conflict of interest.

Keywords: aluminum · Jahn–Teller effect · $Na_{0.67}MnO_2$ · sodium-ion batteries · solid-state NMR spectroscopy

How to cite: *Angew. Chem. Int. Ed.* **2019**, *58*, 18086–18095
Angew. Chem. **2019**, *131*, 18254–18263

[1] a) R. Schmuch, R. Wagner, G. Hörpel, T. Placke, M. Winter, *Nat. Energy* **2018**, *3*, 267–278; b) M. S. Whittingham, *Chem. Rev.* **2014**, *114*, 11414–11443.
[2] a) P. K. Nayak, L. Yang, W. Brehm, P. Adelhelm, *Angew. Chem. Int. Ed.* **2018**, *57*, 102–120; *Angew. Chem.* **2018**, *130*, 106–126; b) T. M. Gür, *Energy Environ. Sci.* **2018**, *11*, 2696–2767.
[3] K. Kubota, N. Yabuuchi, H. Yoshida, M. Dahbi, S. Komaba, *MRS Bull.* **2014**, *39*, 416–422.
[4] a) P.-F. Wang, Y. You, Y.-X. Yin, Y.-G. Guo, *Adv. Energy Mater.* **2018**, *8*, 1701912; b) K. Kubota, S. Kumakura, Y. Yoda, K. Kuroki, S. Komaba, *Adv. Energy Mater.* **2018**, *8*, 1703415.
[5] A. Mendiboure, C. Delmas, P. Hagenmuller, *J. Solid State Chem.* **1985**, *57*, 323–331.

[6] a) J.-P. Parant, R. Olazcuaga, M. Devalette, C. Fouassier, P. Hagenmuller, *J. Solid State Chem.* **1971**, *3*, 1 – 11; b) C. Delmas, C. Fouassier, P. Hagenmuller, *Physica B + C* **1980**, *99*, 81 – 85.
[7] a) R. J. Clément, P. G. Bruce, C. P. Grey, *J. Electrochem. Soc.* **2015**, *162*, A2589 – A2604; b) X. Ma, H. Chen, G. Ceder, *J. Electrochem. Soc.* **2011**, *158*, A1307.
[8] L. Bordet-Le Guenne, P. Deniard, P. Biensan, C. Siret, R. Brec, *J. Mater. Chem.* **2000**, *10*, 2201 – 2206.
[9] S. Kumakura, Y. Tahara, K. Kubota, K. Chihara, S. Komaba, *Angew. Chem. Int. Ed.* **2016**, *55*, 12760 – 12763; *Angew. Chem.* **2016**, *128*, 12952 – 12955.
[10] a) A. R. Armstrong, P. G. Bruce, *Nature* **1996**, *381*, 499 – 500; b) F. Capitaine, P. Gravereau, C. Delmas, *Solid State Ionics* **1996**, *89*, 197 – 202.
[11] A. Caballero, L. Hernán, J. Morales, L. Sánchez, J. Santos Peña, M. A. G. Aranda, *J. Mater. Chem.* **2002**, *12*, 1142 – 1147.
[12] a) M. Guignard, C. Didier, J. Darriet, P. Bordet, E. Elkaim, C. Delmas, *Nat. Mater.* **2013**, *12*, 74 – 80; b) X. Li, X. Ma, D. Su, L. Liu, R. Chisnell, S. P. Ong, H. Chen, A. Toumar, J. C. Idrobo, Y. Lei, J. Bai, F. Wang, J. W. Lynn, Y. S. Lee, G. Ceder, *Nat. Mater.* **2014**, *13*, 586 – 592; c) X. Wu, J. Guo, D. Wang, G. Zhong, M. J. McDonald, Y. Yang, *J. Power Sources* **2015**, *281*, 18 – 26; d) Y. Sun, S. Guo, H. Zhou, *Energy Environ. Sci.* **2019**, 12, 825 – 840.
[13] S. Kumakura, Y. Tahara, S. Sato, K. Kubota, S. Komaba, *Chem. Mater.* **2017**, *29*, 8958 – 8962.
[14] a) J. Billaud, G. Singh, A. R. Armstrong, E. Gonzalo, V. Roddatis, M. Armand, T. Rojo, P. G. Bruce, *Energy Environ. Sci.* **2014**, *7*, 1387 – 1391; b) R. J. Clément, J. Billaud, A. R. Armstrong, G. Singh, T. Rojo, P. G. Bruce, C. P. Grey, *Energy Environ. Sci.* **2016**, *9*, 3240 – 3251; c) N. Sharma, N. Tapia-Ruiz, G. Singh, A. R. Armstrong, J. C. Pramudita, H. E. A. Brand, J. Billaud, P. G. Bruce, T. Rojo, *Chem. Mater.* **2015**, *27*, 6976 – 6986; d) N. Yabuuchi, R. Hara, K. Kubota, J. Paulsen, S. Kumakura, S. Komaba, *J. Mater. Chem. A* **2014**, *2*, 16851 – 16855.
[15] a) M. S. Kwon, S. G. Lim, Y. Park, S. M. Lee, K. Y. Chung, T. J. Shin, K. T. Lee, *ACS Appl. Mater. Interfaces* **2017**, *9*, 14758 – 14768; b) L. Yang, X. Li, X. Ma, S. Xiong, P. Liu, Y. Tang, S. Cheng, Y.-Y. Hu, M. Liu, H. Chen, *J. Power Sources* **2018**, *381*, 171 – 180; c) N. Yabuuchi, R. Hara, M. Kajiyama, K. Kubota, T. Ishigaki, A. Hoshikawa, S. Komaba, *Adv. Energy Mater.* **2014**, *4*, 1301453.
[16] a) T. R. Chen, T. Sheng, Z. G. Wu, J. T. Li, E. H. Wang, C. J. Wu, H. T. Li, X. D. Guo, B. H. Zhong, L. Huang, S. G. Sun, *ACS Appl. Mater. Interfaces* **2018**, *10*, 10147 – 10156; b) W. Kang, Z. Zhang, P.-K. Lee, T.-W. Ng, W. Li, Y. Tang, W. Zhang, C.-S. Lee, D. Y. Wai Yu, *J. Mater. Chem. A* **2015**, *3*, 22846 – 22852.
[17] S. R. Taylor, *Geochim. Cosmochim. Acta* **1964**, *28*, 1273 – 1285.
[18] Y.-R. Luo, *Comprehensive handbook of chemical bond energies*, CRC press, Boca Raton, FL, **2007**.
[19] W.-L. Pang, X.-H. Zhang, J.-Z. Guo, J.-Y. Li, X. Yan, B.-H. Hou, H.-Y. Guan, X.-L. Wu, *J. Power Sources* **2017**, *356*, 80 – 88.
[20] C. Vaalma, D. Buchholz, S. Passerini, *J. Power Sources* **2017**, *364*, 33 – 40.
[21] a) I. Hasa, S. Passerini, J. Hassoun, *J. Mater. Chem. A* **2017**, *5*, 4467 – 4477; b) X. H. Zhang, W. L. Pang, F. Wan, J. Z. Guo, H. Y. Lu, J. Y. Li, Y. M. Xing, J. P. Zhang, X. L. Wu, *ACS Appl. Mater. Interfaces* **2016**, *8*, 20650 – 20659; c) D. W. Han, J. H. Ku, R. H. Kim, D. J. Yun, S. S. Lee, S. G. Doo, *ChemSusChem* **2014**, *7*, 1870 – 1875; d) W. Zhao, H. Kirie, A. Tanaka, M. Unno, S. Yamamoto, H. Noguchi, *Mater. Lett.* **2014**, *135*, 131 – 134.
[22] B. H. Toby, *J. Appl. Crystallogr.* **2001**, *34*, 210 – 213.
[23] J. Xu, D. H. Lee, R. J. Clément, X. Yu, M. Leskes, A. J. Pell, G. Pintacuda, X.-Q. Yang, C. P. Grey, Y. S. Meng, *Chem. Mater.* **2014**, *26*, 1260 – 1269.
[24] A. A. Savina, V. A. Morozov, A. L. Buzlukov, I. Y. Arapova, S. Y. Stefanovich, Y. V. Baklanova, T. A. Denisova, N. I. Medvedeva, M. Bardet, J. Hadermann, B. I. Lazoryak, E. G. Khaikina, *Chem. Mater.* **2017**, *29*, 8901 – 8913.
[25] a) J. Billaud, R. J. Clement, A. R. Armstrong, J. Canales-Vazquez, P. Rozier, C. P. Grey, P. G. Bruce, *J. Am. Chem. Soc.* **2014**, *136*, 17243 – 17248; b) H. Duncan, B. Hai, M. Leskes, C. P. Grey, G. Chen, *Chem. Mater.* **2014**, *26*, 5374 – 5382.
[26] L. Yang, X. Li, J. Liu, S. Xiong, X. Ma, P. Liu, J. Bai, W. Xu, Y. Tang, Y. Y. Hu, M. Liu, H. Chen, *J. Am. Chem. Soc.* **2019**, *141*, 6680 – 6689.
[27] R. J. Clément, J. Xu, D. S. Middlemiss, J. Alvarado, C. Ma, Y. S. Meng, C. P. Grey, *J. Mater. Chem. A* **2017**, *5*, 4129 – 4143.

Manuscript received: September 12, 2019
Accepted manuscript online: October 6, 2019
Version of record online: October 30, 2019

